Single-crystal metal growth on amorphous insulating substrates

Kai Zhang[a,1], Xue Bai Pitner[a,1], Rui Yang[a], William D. Nix[b,2], James D. Plummer[a], and Jonathan A. Fan[a,2]

[a]Department of Electrical Engineering, Stanford University, Stanford, CA 94305; and [b]Department of Materials Science and Engineering, Stanford University, Stanford, CA 94305

Contributed by William D. Nix, December 1, 2017 (sent for review October 12, 2017; reviewed by Hanchen Huang, David J. Srolovitz, and Carl Thompson)

Metal structures on insulators are essential components in advanced electronic and nanooptical systems. Their electronic and optical properties are closely tied to their crystal quality, due to the strong dependence of carrier transport and band structure on defects and grain boundaries. Here we report a method for creating patterned single-crystal metal microstructures on amorphous insulating substrates, using liquid phase epitaxy. In this process, the patterned metal microstructures are encapsulated in an insulating crucible, together with a small seed of a differing material. The system is heated to temperatures above the metal melting point, followed by cooling and metal crystallization. During the heating process, the metal and seed form a high-melting-point solid solution, which directs liquid epitaxial metal growth. High yield of single-crystal metal with different sizes is confirmed with electron backscatter diffraction images, after removing the insulating crucible. Unexpectedly, the metal microstructures crystallize with the ⟨111⟩ direction normal to the plane of the film. This platform technology will enable the large-scale integration of high-performance plasmonic and electronic nanosystems.

single-crystal metal | liquid phase epitaxy | solid-state diffusion | gold | microcrucible

High-quality metals are essential for obtaining desirable electronic and nanooptical properties in metal structures and devices. For many of these properties, the elimination of grain boundaries results in dramatic enhancements. In electronics, single-crystal metal structures have higher electrical conductivity and are more resistant to electromigration compared with polycrystalline structures (1–4). In plasmonics, single-crystal metal devices possess exceptional plasmon propagation lengths (5) and electromagnetic field enhancements, which enable high-performance waveguides (6, 7), sensors (8), antennas (9), and metamaterials (10, 11). Metal crystal quality also plays a major role in catalysis (12, 13), photodetection (14, 15), energy harvesting (16, 17), and flexible electronics (18) due to the dependence of hot carrier dynamics, molecular kinetics, and mechanical properties on defects and crystal orientation.

There currently exist two general routes to fabricating single-crystal metal structures on substrates. The first is to grow lattice-matched metal films onto crystalline substrates using molecular beam epitaxy (19–21), electrodeposition, or physical vapor deposition (10, 11, 22) processes. These techniques are limited to the use of either nonelectrically insulating or nonconventional substrate materials. The second is to chemically grow single-crystal metal colloids in solution (7–9, 23) and cast the structures onto a substrate, which cannot readily generalize to the construction of large-area integrated systems. To scientifically and technologically unlock the full potential of thin-film metal structures, we require new top-down techniques that can produce single-crystal metal structures on amorphous insulating substrates, bypassing the requirement for direct contact with single-crystal substrates, and with shapes and positions patterned by lithography. Compatibility with substrate materials such as silicon dioxide is critical for applications that require electrical isolation and a low refractive index background.

Our method is based on liquid phase epitaxy, in which the polycrystalline metal structures are encapsulated in an amorphous insulating crucible, together with polycrystalline seed structures of differing material, and heated to the liquid phase. As the system cools, the metal solidifies into single crystals. Liquid phase epitaxy has been previously studied in the context of semiconductor-on-oxide growth (24–26), but has not been explored for metal growth. We will examine gold as a model system in this study. Gold is an essential material in electronics and plasmonics because of its high conductivity and chemical inertness. We use platinum as our seed material, which has a high melting temperature and forms an isomorphous binary phase diagram with gold, with a miscibility gap at lower temperatures.

Results and Discussion

The device layout and fabrication flow are outlined in Fig. 1 *A* and *B*. To quantify crystal orientations and grain sizes in our samples, we use electron backscatter diffraction (EBSD) imaging. Representative, large-area EBSD images of gold microstripes are presented in Fig. 1*C*, together with a scanning electron microscopy (SEM) image of an individual stripe. The yield of single crystals for the 20 devices in the image is 100%. Interestingly, the orientations of the metal crystals are not random but have the ⟨111⟩ direction perpendicular to the substrate (i.e., along the *z* axis in the EBSD images; see coordinates in Fig. 1*C*). In the directions along (*x* axis) and transverse (*y* axis) to the stripe, the crystal orientations are random (*SI Appendix*, Fig. S1). Our process generally applies to a

Significance

Eliminating grain boundaries of metal structures is desirable for many electronic and nanooptical applications. However, a technique that can be used to grow large-scale patterned single-crystal metal on amorphous insulating substrate has not been demonstrated. In this work, we show that using liquid phase epitaxy, microstructures of single-crystal metal can be grown on amorphous insulating substrates such as silicon dioxide with high yield. The single-crystal metal can be further patterned on the insulating substrate with lithography into functional devices, which avoids the transfer, and is largely scalable. This technology platform will reduce the failure of metal structures in electronic systems, and enable more efficient plasmonic nanostructures.

Author contributions: K.Z., X.B.P., R.Y., J.D.P., and J.A.F. designed research; K.Z., X.B.P., R.Y., J.D.P., and J.A.F. performed research; K.Z., X.B.P., R.Y., W.D.N., J.D.P., and J.A.F. analyzed data; and K.Z., X.B.P., R.Y., W.D.N., J.D.P., and J.A.F. wrote the paper.

Reviewers: H.H., Northeastern University; D.J.S., University of Pennsylvania; and C.T., Massachusetts Institute of Technology.

The authors declare no conflict of interest.

Published under the PNAS license.

[1]K.Z. and X.B.P. contributed equally to this work.

[2]To whom correspondence may be addressed. Email: nix@stanford.edu or jonfan@stanford.edu.

This article contains supporting information online at www.pnas.org/lookup/suppl/doi:10.1073/pnas.1717882115/-/DCSupplemental.

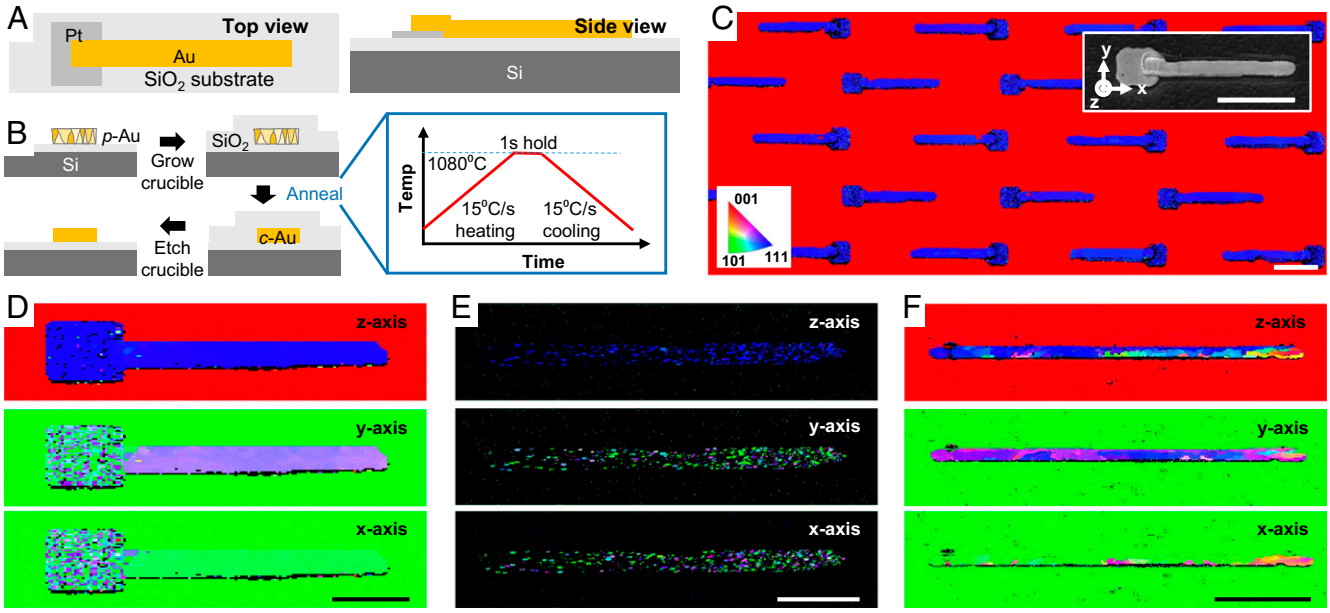

Fig. 1. Liquid metal epitaxy process with gold microstripes and platinum seed structures. (*A*) Schematic of the structures before processing. (*B*) Schematic of the fabrication process flow. The images are cross-sectional views of the gold stripe away from the platinum seed region. (*Inset*) Diagram of the annealing parameters. (*C*) Large-area EBSD image of processed gold stripes. The color map (*Lower Left*) describes the orientations of the crystal plane normals. (*Inset*) SEM image of an individual gold stripe. The coordinate system denotes the axes for EBSD analysis: *x* axis along the stripe, *y* axis transverse to the stripe, and *z* axis normal to the stripe and substrate. (Scale bars: 20 μm.) (*D*) EBSD images of a representative processed gold stripe with platinum seed. (*E*) EBSD images of a representative gold stripe, as deposited by electron beam evaporation. (*F*) EBSD images of a representative gold stripe with no platinum seed, processed using the annealing parameters in *B*. (Scale bars for *D*–*F*: 10 μm.)

broad range of microstructures, including stripes of tens to hundreds of micrometers length and branch-like structures (*SI Appendix*, Figs. S2–S5). In devices that did not produce single crystals, we observe microcrucible warping or failure, and we anticipate higher overall yield by using thicker and stiffer microcrucibles.

Detailed EBSD images of a representative processed gold microstripe are presented in Fig. 1*D* and show that the seed region, defined by the area of overlapping gold and platinum, is polycrystalline with a ⟨111⟩ fiber texture. A closer examination of the EBSD images reveals slight color variation of the gold microstripe, indicative of some minor variations in orientation. We also perform an EBSD analysis on two control samples. The first is of an as-deposited gold stripe without encapsulation or annealing (Fig. 1*E*). This stripe is polycrystalline with grains oriented with ⟨111⟩ directions normal to the plane of the film, which is consistent with the ⟨111⟩ fiber textures observed for vapor-deposited face-centered-cubic (fcc) metal films on glass substrates (27). The second is of a processed gold sample with no platinum seed (Fig. 1*F*). This stripe is polycrystalline with randomly oriented grains, indicating that upon system cooling, the liquid gold crystallized with multiple random nucleation points and crystal orientations. As such, the platinum seed is essential to producing single-crystal gold structures.

A representative transmission electron microscopy (TEM) image of a gold microstripe cross-section, with the top section of the oxide crucible etched away, is presented in Fig. 2. This 2.4-μm-long film section possesses constant thickness and smooth sidewalls at the gold–silicon dioxide and gold–air interfaces. Diffraction patterns from three different sections of the stripe all show the same pattern and orientation, confirming that the sample is an fcc single crystal. The nonuniform brightness within the diffraction spots is due to standard dynamical scattering effects. High-resolution images of the gold stripe at the gold–silicon dioxide and gold–air interfaces (Fig. 2*B*) show clear lattice fringes oriented along the length of the crucible, which represent (111) planes. The spacing between fringes is measured to be

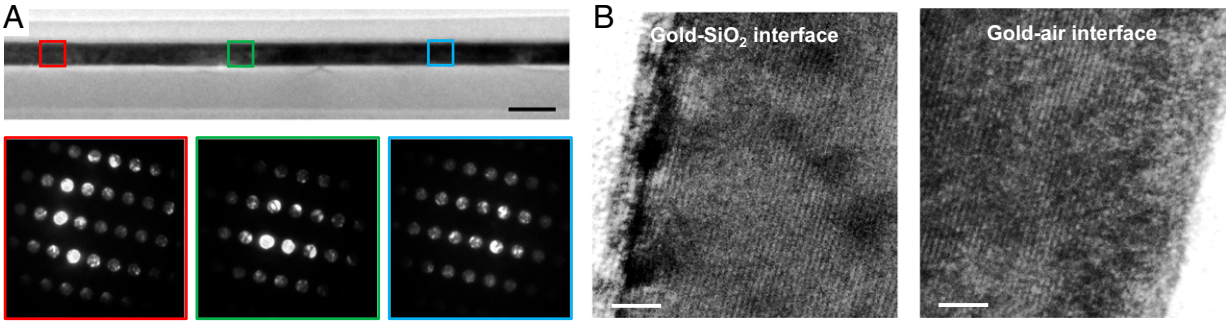

Fig. 2. High-resolution TEM analysis of crystallized gold microstripes. (*A*) TEM image of a section of a processed gold microstripe. Diffraction patterns from three sections of the microstripe show that the sample is an fcc single crystal. (Scale bar: 200 nm.) (*B*) High-resolution TEM images of the gold–silicon dioxide and gold–air interfaces. The lattice fringes are (111) planes in the gold crystal and are due to the crystallinity of the gold. (Scale bar: 2 nm.)

0.235 nm, precisely matching the expected spacing between (111) planes in the fcc gold lattice with a lattice parameter of 0.407 nm.

The mechanism behind single-crystal growth originates with the layered gold–platinum seed structure. A TEM cross-sectional image of the postannealed seed region (Fig. 3*A*) reveals that the gold and platinum layers, which were separate layers before annealing, form a gold–platinum solid solution after annealing. An elemental map, constructed using energy-dispersive spectroscopy (EDS), shows that gold and platinum are distributed uniformly across the width of the cross-section (Fig. 3*A*, *Inset*). Furthermore, the solid solution has a $Pt_{0.23}Au_{0.77}$ composition, which contains mass fractions of gold and platinum that are approximately those of the metals in the seed region before annealing. We conclude that as the sample is heated, the gold and platinum undergo solid-state interdiffusion. This gold–platinum alloy remains a solid throughout the annealing process because it has a higher melting point than the maximum annealing temperature (1,080 °C), as visualized in the gold–platinum phase diagram (Fig. 3*B*).

A further examination of the solid-state diffusion process indicates that the uniform gold–platinum seed structure forms at relatively low temperatures. To quantify metal interdiffusion, we use a partial differential equation model, which is described in detail in *Materials and Methods*. The model accounts for the 15 °C/s rate of heating and captures the nonequilibrium diffusion dynamics of the system. The cross-sectional material profile within the seed as a function of temperature is plotted in Fig. 3*C* and displays spatially separate gold and platinum regions at low temperatures. Near 500 °C, metal diffusion across the gold–platinum boundary becomes noticeable, and by 800 °C the two metal types have completely interdiffused, forming a $Pt_{0.23}Au_{0.77}$ alloy. As such, the solid seed alloy forms well below the melting point of gold. These results are corroborated in experiments where 80-nm-thick gold and 30-nm-thick platinum seed structures are heated to 900 °C, well below the gold melting point. TEM cross-sectional images and EDS maps of these postannealed structures (Fig. 3*D*) reveal a uniform alloy, with a stoichiometry similar to that of the preannealed seed region composition.

Detailed EBSD images of the postannealed gold–platinum seeds show that the seed is polycrystalline, and that its grains have ⟨111⟩ directions perpendicular to the substrate (Fig. 3*E*). The source for such orientation alignment can be traced back to the crystallinity of the as-deposited seeds, which possess a ⟨111⟩ fiber texture (Fig. 1*E*). The (111) crystal orientation is preserved as the seed is annealed because it remains a solid throughout the metal interdiffusion process. Liquid epitaxial gold growth originates from a single grain in the seed region (Fig. 3*E*, white arrows), which determines the crystal orientation of the gold stripe. The gold stripe is oriented with the ⟨111⟩ direction along the *z* axis because all of the grains in the seed region possess this crystal orientation. Along the *x*-and *y* axes, the orientation of the gold stripe is random because the grain orientations in the seed region are random along these axes (*SI Appendix*, Fig. S6). In systems with wider widths, multiple competing crystal-growth processes can be visualized at the boundary of the seed region and gold stripe (*SI Appendix*, Fig. S7), demonstrating that gold epitaxial growth originates from grains in the seed region.

Gold epitaxy occurs at the gold–seed interface due to the low interfacial energy between gold and the seed grains. This low interfacial energy arises because gold and platinum both have fcc lattices, have similar lattice parameters with only a 4% mismatch, and have thermodynamic interactions specified by an isomorphous binary phase diagram where the solidus and liquidus

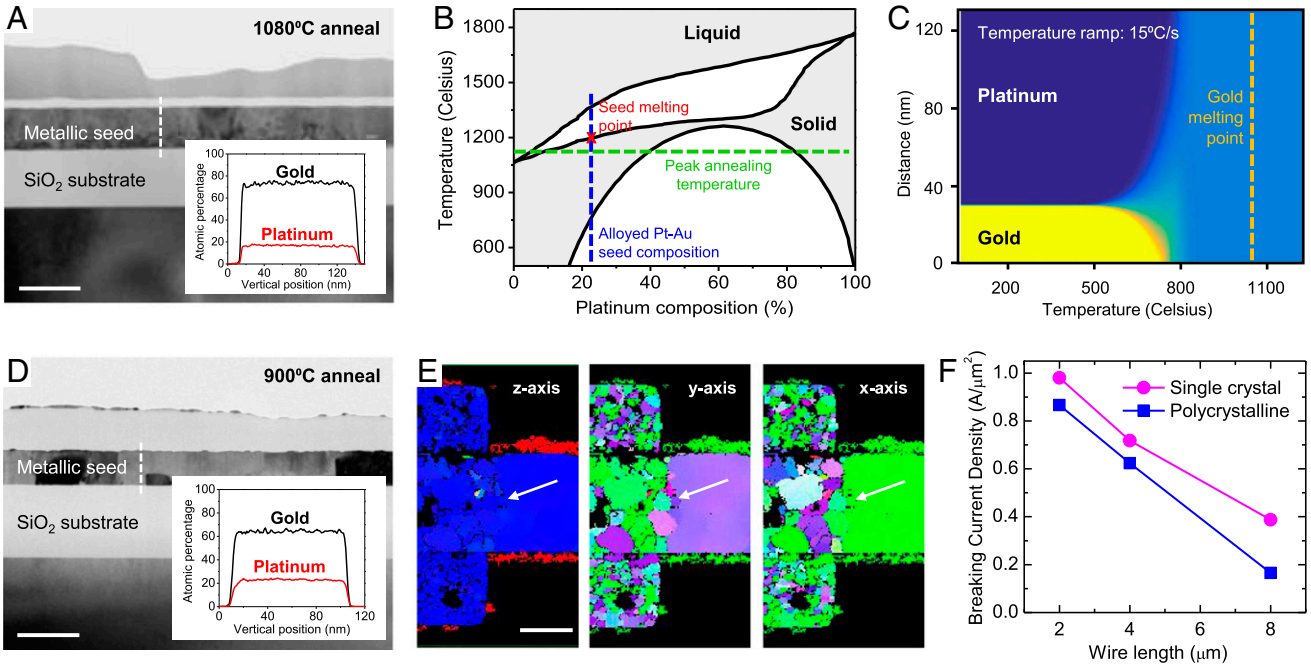

Fig. 3. Materials analysis of the gold–platinum seed region. (*A*) TEM image of a cross-section of the seed region, after annealing at 1,080 °C. (*Inset*) Distribution of gold and platinum within a vertical cut of the sample (white dashed line), measured by EDS. (Scale bar: 200 nm.) (*B*) Platinum–gold binary phase diagram. The peak temperature from the annealing process is signified by a dashed green line. The composition of the alloyed platinum–gold seed region is signified by the rightmost blue dashed line. The melting point of such a material is above the green line. (*C*) Calculated cross-sectional distribution of platinum and gold within the seed region as a function of temperature. (*D*) TEM image of a cross-section of the seed region, after annealing at 900 °C. (*Inset*) Distribution of gold and platinum within a vertical cut of the sample (white dashed line), measured by EDS. (Scale bar: 200 nm.) (*E*) EBSD images of the platinum–gold seed region of a representative sample after annealing. The *z*-axis image shows that the seed region and gold stripes have a ⟨111⟩ fiber texture. The white arrows point to the gold–platinum grain that serves as the site for liquid phase epitaxy. (*F*) Plot of breaking current density, which signifies electrical breakdown, for single-crystal and polycrystalline gold wires of differing length.

temperatures both increase with Pt content. As such, the kinetics for epitaxial growth at the seed are much faster than those of competing events, such as the nucleation of gold crystals at the walls of the crucible. This observation, together with the rest of our analysis, provides a pathway to generalizing our system to other metal combinations. As a proof of concept, we have prepared samples consisting of a gold stripe and palladium seed. Gold and palladium both have fcc lattices and an isomorphous binary phase diagram with solidus and liquidus temperatures increasing with Pd content. These samples produce single-crystal gold stripes upon processing (*SI Appendix*, Fig. S7). We also show that single crystals of gold can be grown in an insulating silicon nitride crucible (*SI Appendix*, Fig. S8).

To demonstrate the enhanced electronic properties of single-crystal metal structures prepared using our method, we characterize the tolerance of single-crystal gold wires to electrical breakdown and compare them to as-deposited polycrystalline gold wires. For each wire, electrical contacts are made and the current is swept until device failure (see *SI Appendix*, Fig. S9 and *Materials and Methods* for details). Fig. 3*F* plots the breaking current density, which signifies device failure, for gold wires of differing length. Differences in the breaking current density as a function of wire length are due to thermal transport at the electrode pads and compressive mechanical stresses that arise from metal ion transport (28). The plot generally shows that the single-crystal wires have higher thresholds to failure than those made from polycrystalline gold, and that for 8-μm-long single-crystal wires, the critical current density is over twice that of its polycrystalline counterpart. As such, the elimination of grain boundaries enhances the threshold of single-crystal gold wires to electrical breakdown.

In conclusion, we have identified a route to processing metal structures on amorphous insulating substrates into oriented single crystals. Our understanding of the crystal metal growth mechanism is summarized in Fig. 4. The method is entirely compatible with standard fabrication processes, including lithography and damascene patterning, making it a practical route toward large-area wafer-scale devices. We predict that this concept can generalize to the single-crystal processing of metals beyond gold, pending the proper choice of metal, seed, and crucible materials. In particular, the crystal-growth process we have discovered relies on the Pt–Au seed remaining solid when the Au is in the liquid state. This occurs because the liquidus and solidus temperatures at the Au-rich end of the Au–Pt phase diagram increase with Pt content. This suggests that other stripe-seed combinations with increasing liquidus and solidus temperatures, such as Cu–Pt, Cu–Pd, Ag–Pt, and Ag–Pd, might permit this process to be used to create single-crystal stripes of Cu or Ag. The prospect for creating single-crystal Al stripes by this process are not promising as the liquidus and solidus temperatures decrease with solute content for all solutes. Other schemes would have to be invented to create single-crystal Al stripes. We envision that this material growth technique will enable electronic and plasmonic systems operating at the material performance limits of metals.

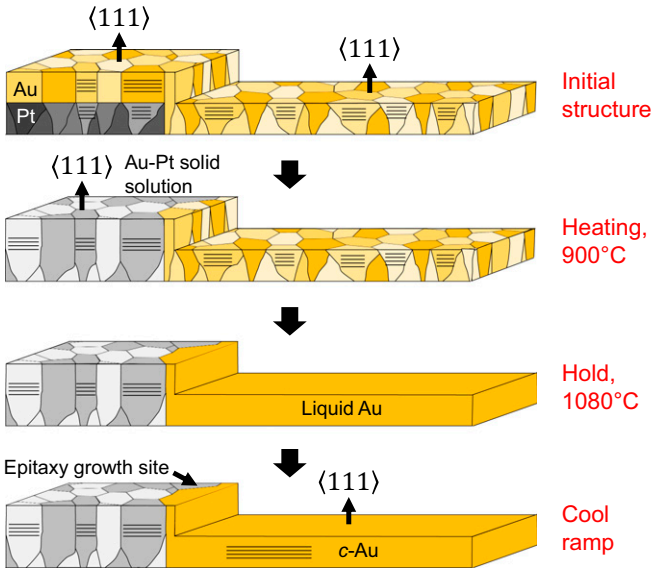

Fig. 4. Schematic of the liquid phase epitaxy process. As the sample is heated, a high-melting-point seed consisting of a gold–platinum solid solution forms before the melting of gold. As the temperature reaches 1,080 °C, the gold in the stripe liquefies. Upon cooling, one of the grains in the gold–platinum solid solution serves as a site for liquid phase epitaxy, and a growth front propagates rapidly through the crucible.

Materials and Methods

Fabrication Process. The substrates used in these experiments were (100) single-crystal p-type Si substrates. The bottom layer of the microcrucible was prepared by growing one of two types of thin films on the silicon substrate: thermal oxide layers were grown at 950 °C and low-pressure chemical vapor deposition (LPCVD) Si_3N_4 layers were grown at 800 °C. The thicknesses of these films varied from 50 to 200 nm.

Next, the seed and stripe layers were patterned. Conventional photolithography with a 1-μm-thick positive photoresist was performed to pattern the seed, and a 30-nm-thick platinum or palladium metal film was deposited using electron beam evaporation. The sample was soaked in acetone for metal lift-off. A second lithography step was used for gold stripe patterning. After photoresist development, a 100-nm-thick gold metal film was deposited using electron beam evaporation, followed by soaking in acetone for metal lift-off. The gold stripes had lengths ranging from 10 to 200 μm and widths ranging from 4 to 40 μm. The seeds were 10 μm long, and each seed was 6 μm wider than its associated stripe. The stripes overlapped lengthwise with the seeds by 3 μm.

Following metal deposition, a 1-μm-thick LPCVD SiO_2 layer, grown at 300 °C, was deposited on the sample surface to serve as the top layer of the microcrucible. Heating was performed using rapid thermal annealing. The temperatures in the furnace were calibrated using a pyrometer. The samples were heated with a ramp rate up of 15 °C/s to 1,080 °C, held for 1 s, and then cooled with a ramp rate of 15 °C/s. The ramp rates were set by controlling the intensity of the lamp heater. After annealing, the SiO_2 capping layer was removed through dry plasma etching. For Fig. 1 *C*, *D*, and *F*, the underlying thermal oxide layer was also etched through, exposing the underlying crystalline silicon substrate (red and green background in the EBSD images).

For the electrical breakdown experiments, 800-nm-wide gold wires were defined in the gold microstripes using electron beam lithography, followed by argon ion milling. The contact pads were patterned by optical lithography, followed by the deposition of a 2-nm-thick titanium adhesion layer and 200-nm-thick gold layer, and then metal lift-off. Electrical measurements were performed with a Keithley 4200 SCS semiconductor parameter analyzer and a probe station. Current was swept in each wire in steps of 1 mA, and held for 1 s at each step, while the voltage was continuously monitored. Electrical breakdown was signified when the voltage suddenly increased to the compliance voltage.

Diffusivity Modeling. Solid-state diffusion between Au and Pt occurs at the seed region where the Au stripe overlaps with the Pt seed during the heating cycle. The solid-state interdiffusion of Au and Pt is significant enough that the seed region becomes a uniform Pt_xAu_{1-x} alloy before melting begins. Pt and Au are mutually soluble but chemically different. The partial differential equation describing this interdiffusion behavior is

$$\frac{\partial x_{Pt}}{\partial t} = \frac{\partial}{\partial z}\left[\left(x_{Au}D_{Pt} + x_{Pt}D_{Au}\right)\frac{\partial x_{Pt}}{\partial z}\right],$$

where x_{Pt} is the fraction of Pt material in the system, x_{Au} is the fraction of Au material in the system, z is the distance from the bottom of the seed, D_{Pt} is the diffusivity of Pt material in pure Au, and D_{Au} is the diffusivity of Au in pure Pt (29). Since the system consists of only Pt and Au, the fractions relate as

$$x_{Au} = 1 - x_{Pt}.$$

Therefore, the partial differential equation can be expressed as

$$\frac{\partial x_{\mathrm{Pt}}}{\partial t} = (D_{\mathrm{Au}} - D_{\mathrm{Pt}})\left(\frac{\partial x_{\mathrm{Pt}}}{\partial z}\right)^2 + (D_{\mathrm{Pt}} + x_{\mathrm{Pt}} \cdot (D_{\mathrm{Au}} - D_{\mathrm{Pt}}))\frac{\partial^2 x_{\mathrm{Pt}}}{\partial z^2}.$$

At time 0, the stripe material and seed material have not mixed. The initial conditions are

$$x_{Pt}(0, z) = \begin{cases} 1 & 0 < z \leq \mathrm{seed}_H \\ 0 & \mathrm{seed}_H < z \leq \mathrm{seed}_H + \mathrm{stripe}_H \end{cases},$$

where stripe_H is the total thickness of the Au stripe and seed_H is the thickness of the Pt seed.

At any point during the annealing process, there is no flux of material diffusing through the bottom of the seed nor the top of the stripe. The boundary conditions are therefore

$$(D_A + (D_B - D_A) \cdot x_A(t, 0))\frac{\partial x_A(t, 0)}{\partial z} = 0,$$

$$(D_A + (D_B - D_A) \cdot x_A(t, \mathrm{stripe}_H + \mathrm{seed}_H))\frac{\partial x_A(t, \mathrm{stripe}_H + \mathrm{seed}_H)}{\partial z} = 0.$$

To solve the partial differential equation (PDE), we used the PDE solver in MATLAB. The temperature ramp rate is 15 °C/s.

ACKNOWLEDGMENTS. K.Z., X.B.P., R.Y., and J.A.F. acknowledge A. Marshall for TEM support, R. Chin for EBSD support, and S. Doshay for fabrication assistance. J.A.F. acknowledges support from the Air Force Office of Scientific Research Multidisciplinary University Research Initiative under Award FA9550-16-1-0031, the National Science Foundation under Award 1608525, and the Alfred P. Sloan Foundation. K.Z. acknowledges support from the Stanford Graduate Fellowship.

1. Pierce DG, Brusius PG (1997) Electromigration: A review. *Microelectron Reliab* 37:1053–1072.
2. Wu Y, Xiang J, Yang C, Lu W, Lieber CM (2004) Single-crystal metallic nanowires and metal/semiconductor nanowire heterostructures. *Nature* 430:61–65.
3. Mayadas AF, Shatzkes M (1970) Electrical-resistivity model for polycrystalline films: The case of arbitrary reflection at external surfaces. *Phys Rev B* 1:1382–1389.
4. Koo KH, Saraswat KC (2011) Study of performances of low-k Cu, CNTs, and optical interconnects. *Nanoelectronic Circuit Design*, eds Jha NK, Chen D (Springer, New York), pp 377–407.
5. Wu Y, et al. (2014) Intrinsic optical properties and enhanced plasmonic response of epitaxial silver. *Adv Mater* 26:6106–6110.
6. Akimov AV, et al. (2007) Generation of single optical plasmons in metallic nanowires coupled to quantum dots. *Nature* 450:402–406.
7. Ditlbacher H, et al. (2005) Silver nanowires as surface plasmon resonators. *Phys Rev Lett* 95:257403.
8. Sherry LJ, et al. (2005) Localized surface plasmon resonance spectroscopy of single silver nanocubes. *Nano Lett* 5:2034–2038.
9. Huang J-S, et al. (2010) Atomically flat single-crystalline gold nanostructures for plasmonic nanocircuitry. *Nat Commun* 1:150.
10. Fedotov VA, Uchino T, Ou JY (2012) Low-loss plasmonic metamaterial based on epitaxial gold monocrystal film. *Opt Express* 20:9545–9550.
11. High AA, et al. (2015) Visible-frequency hyperbolic metasurface. *Nature* 522:192–196.
12. Awazu K, et al. (2008) A plasmonic photocatalyst consisting of silver nanoparticles embedded in titanium dioxide. *J Am Chem Soc* 130:1676–1680.
13. Borkowska Z, Tymosiak-Zielinska A, Shul G (2004) Electrooxidation of methanol on polycrystalline and single crystal gold electrodes. *Electrochim Acta* 49:1209–1220.
14. Knight MW, Sobhani H, Nordlander P, Halas NJ (2011) Photodetection with active optical antennas. *Science* 332:702–704.
15. Chalabi H, Schoen D, Brongersma ML (2014) Hot-electron photodetection with a plasmonic nanostripe antenna. *Nano Lett* 14:1374–1380.
16. Sundararaman R, Narang P, Jermyn AS, Goddard WA, 3rd, Atwater HA (2014) Theoretical predictions for hot-carrier generation from surface plasmon decay. *Nat Commun* 5:5788.
17. Clavero C (2014) Plasmon-induced hot-electron generation at nanoparticle/metal-oxide interfaces for photovoltaic and photocatalytic devices. *Nat Photonics* 8:95–103.
18. Mahenderkar NK, et al. (2017) Epitaxial lift-off of electrodeposited single-crystal gold foils for flexible electronics. *Science* 355:1203–1206.
19. Cho AY, Dernier PD (1978) Single-crystal-aluminum Schottky-barrier diodes prepared by molecular-beam epitaxy (MBE) on GaAs. *J Appl Phys* 49:3328–3332.
20. Smith AR, Chao K-J, Niu Q, Shih C-K (1996) Formation of atomically flat silver films on GaAs with a "silver mean" quasi periodicity. *Science* 273:226–228.
21. Krogstrup P, et al. (2015) Epitaxy of semiconductor-superconductor nanowires. *Nat Mater* 14:400–406.
22. Palmberg PW, Rhodin TN, Todd CJ (1967) Epitaxial growth of gold and silver on magnesium oxide cleaved in ultrahigh vacuum. *Appl Phys Lett* 11:33–35.
23. Lee Y-J, et al. (2013) Ultrasmooth, highly spherical monocrystalline gold particles for precision plasmonics. *ACS Nano* 7:11064–11070.
24. Liu Y, Deal MD, Plummer JD (2004) High-quality single-crystal Ge on insulator by liquid phase epitaxy on Si substrates. *Appl Phys Lett* 84:2563–2565.
25. Shimura T, et al. (2015) Enhancement of photoluminescence from n-type tensile-strained GeSn wires on an insulator fabricated by lateral liquid phase epitaxy. *Appl Phys Lett* 107:221109.
26. Glaser M, et al. (2016) Synthesis, morphological, and electro-optical characterizations of metal/semiconductor nanowire heterostructures. *Nano Lett* 16:3507–3513.
27. Thompson CV (2000) Structure evolution during processing of polycrystalline films. *Annu Rev Mater Sci* 30:159–190.
28. Arzt E, Nix WD (2011) A model for the effect of line width and mechanical strength on electromigration failure of interconnects with "near-bamboo" grain structures. *J Mater Res* 6:731–736.
29. Liu Y, et al. (2012) Phase boundary migration, Kirkendall marker shift and atomic mobilities in FCC Au–Pt alloys. *Calphad* 36:94–99.